Properties and Physical Interpretation of the Dynamic Interactions between Voltage Source Converters and Grid: Electrical Oscillation and Its Stability Control

Chen Zhang[1*], Xu Cai[1], Zheng Li[1], Atle Rygg[2], Marta Molinas[2]

[1] Department of Wind Power Research Center, Shanghai Jiao Tong University, Shanghai, China

[2] Department of Engineering Cybernetics, Norwegian University of Science and Technology, Trondheim, Norway

*nealbc@sjtu.edu.cn

Abstract: Voltage source converters (VSCs) play an important role in the power conversion of renewable power generation (RPG) systems. Conventional power systems are considerably affected by power electronic devices in systems with a high percentage of RPG. Various abnormal interactions in the form of oscillations between VSCs and grid have been reported, whereas the mechanism still lacks of knowing. In this study, the properties of interactions between the VSC and grid are investigated, consequently the mechanisms of electrical oscillations are revealed. First, a simple *resistance-inductance-capacitance* (RLC) equivalent to the small-signal model of VSC–grid system was derived based on the knowledge of *virtual passive element effects* of VSC. Then, an *intrinsic oscillatory point* (IOP) in the *RLC* circuit was found, the damping characteristics of the current controller and phase-locked loop at this point were analysed. Subsequently, a *critical stability criterion* for the determination of PLL bandwidth that may trigger oscillations was established. For the improvement of the overall damping, a VSC stabiliser was put forward. Finally, the mechanism analysis and analytical criteria were verified by time domain simulations in PSCAD/EMTDC.

1. Introduction

Voltage source converters (VSCs) are widely used in power conversion and grid integration of renewable power generation (RPG) systems, such as solar [1] and wind power generation systems [1]. The dynamics of conventional power systems are considerably affected by the power electronic devices in systems with a high percentage of RPG. This condition leads to a variety of abnormal interactions, such as harmonic oscillations [3, 4], sub-synchronous oscillations (SSO) [5, 6] or electrical oscillations [6],

between the VSC-based RPG system and grid. Compared with the rotor-angle oscillations in a synchronous generator-based power system, the dynamic interactions between the VSC-based RPG system and grid present wide frequency scales and complex mechanisms. Therefore, the dynamic properties introduced by VSCs and their effects on system stability should be elucidated.

Linearized state-space models and frequency-dependent models are normally used to analyse the small-signal stability of VSC-based systems. However, both of them have certain advantages and disadvantages. A frequency-dependent model of VSCs can be in the form of an admittance [7], sequence impedance [8] or *dq* impedance model [9]. The interconnected system (VSC–grid) can be divided into source and load equivalents; consequently, the classical Nyquist criterion [10] for a sequence impedance model or the general Nyquist criterion (GNC) [11] for a *dq* impedance model can be implemented to assess system stability. This set-up has been successfully applied to detect harmonic [12] and low-frequency oscillations [14, 15] as well as micro grid instability [15]. Oscillation mitigation methods were developed in [16] and [17] on the basis of the knowledge of impedance characteristics. However, impedance models are not directly applied to control system design because of the poor representation of internal variables. In addition, Nyquist criterion only shows numerical results, and it can hardly reveal the relationship between stability and the system variables. By contrast, modal analysis [18] based on a state-space model is superior in this respect as it uses participation factors (PFs) [19] and sensitivity analysis tools [20]. A detailed state-space model and modal analysis process for doubly fed induction generators of wind farms are presented in [21] and [22]. However, state-space models can encounter numerical issues [23] when calculating system eigenvalues, particularly for highly stiff systems (e.g. VSC-based power systems). Additionally, detailed information on the parameter values of the entire system is required, and these values are usually difficult to obtain. On the contrary, an impedance model can be obtained by on-line frequency scanning even if the system parameters are unknown [25–27].

Impedance models and state-space models for VSCs are effective for stability analysis, but both of them present difficulties in physically interpreting instability. In this respect, another method referred to as *complex torque coefficient approach* can be used to model the system by a *speed* and *torque* equivalence. Therefore, the instability of the system can be physically interpreted as *speed* instability. This approach is extensively used to elucidate the mechanism of SSOs in High-Voltage-DC systems [28, 29] and torsional

dynamics in turbine-generator units [29]. An improved method for multi-machine systems is presented in [30].

In general, VSC-based RPG systems can actively interact with the grid, which may lead to stability issues. However, research dedicated to the properties and physical interpretation of the instability phenomenon is limited. Thus, this paper aims to investigate the mechanism of the electrical oscillations in VSC–grid systems. The remainder of this paper is organised as follows: in Section 2, a typical grid-tied VSC system is presented. Then, a reduced-order model for the dynamic property analysis of the VSC under strong grid conditions is derived. In Section 3, the detailed model for the dynamic property analysis of the VSC under weak grid conditions is derived, including the phase-locked loop (PLL), VSC current control and grid dynamics. Subsequently, the intrinsic oscillatory point (IOP) in the VSC–grid system is found, and the critical stability criterion (CSC) for determining the conditions of instability is established. In Section 4, a stabiliser is proposed to enhance the stable operation capability of the VSC. In Section 5, simulations in PSCAD/EMTDC are presented and the validity of the analysis is verified.

2. Dynamic properties of the VSC under strong grid conditions

2.1 Configurations of the VSC–grid system

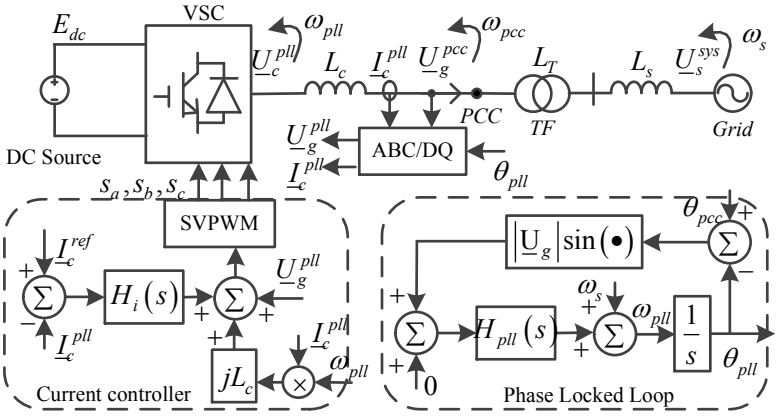

a

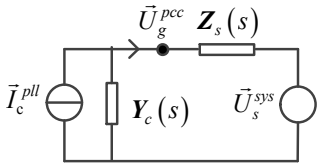

b.

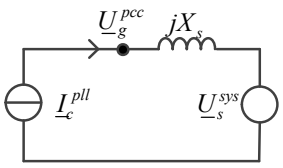

c.

Fig. 1. Schematic and equivalent circuit of the VSC–grid system

a. Schematic of the VSC–grid system

b. Equivalent circuit of the VSC–grid system

c. Equivalent circuit for strong grid analysis

Fig. 1a shows the main circuit of the system constitutes the VSC, AC filter inductor (L_c), step-up transformer and Thévenin equivalent grid. The input filter (e.g. LCL) is eliminated because its dynamics are faster than the scope of this study. The DC link is represented by a constant voltage source because only the current controller is considered. The grid impedance is represented by an inductor (L_s), whereas the resistance is neglected due to the high X/R ratio in the transmission grid, this assumption may lead to slightly conservative stability results. The VSC is synchronised to the grid via a typical PLL and controlled with standard current vector control [7]. The point of common coupling (PCC) is defined at the VSC–grid synchronisation point. Thus, the leakage inductance (L_T) of the step-up transformer can contribute to the short circuit ratio (SCR) and consequently reduce grid stiffness.

Worth to emphasise, three reference frames are introduced in the analysis, i.e., the PLL rotating reference frame (PLL-RF), PCC voltage rotating reference frame (PCC-RF) and synchronously rotating reference frame (SRF). These reference frames are introduced because of modelling consideration. In Fig. 1a, the notations with superscripts *pll*, *pcc* and *sys* represent the vectors in PLL-RF, PCC-RF and SRF respectively, and their corresponding angular speeds are $\omega_{pll}, \omega_{pcc}$ and ω_{sys}. In a steady state, $\omega_{pll} = \omega_{pcc} = \omega_{sys}$.

2.2 Reduced-order model of the VSC–grid system

A typical *dq* impedance model of the VSC–grid system is shown in Fig. 1b. The VSC is represented by a Norton equivalent, whereas the grid is represented by a Thévenin equivalent. Note that the admittance $\mathbf{Y}_c(s)$ of the VSC and the impedance $\mathbf{Z}_s(s)$ of the grid are 2×2 matrices [7]. The existence of $\mathbf{Y}_c(s)$ renders the harmonic currents flow in the VSC, and may trigger harmonic oscillations if $\mathbf{Z}_s(s)$ is large, e.g. LCL oscillation against the weak grid in [17]. In this study, abnormal interactions are interpreted as the *properties of the VSC–grid system under weak grid conditions*. Initially analysing the normal interactions of the VSC–grid system under strong grid can be helpful in the subsequent investigation. Therefore, a reduced-order model of VSC can be derived with the following assumptions:

a) $\mathbf{Y}_c(s) \to 0$, the feed-forwards in the VSC control are ideally compensated grid disturbances.

b) $\mathbf{Z}_s(s) \to j\omega_s L_s$, the grid is quasi-static in accordance with assumption a).

c) $\underline{I}_c^{pll} = \frac{1}{T_c s + 1} \underline{I}_c^{ref}$, the current response is approximated by a first-order transfer function, where T_c is the time constant; $\underline{I}_c^{ref}$ and $\underline{I}_c^{pll}$ are the complex-valued reference and actual current in PLL-RF).

d) $\theta_{pll} = \frac{1}{T_{pll} s + 1} \theta_g$, PLL response is approximated by a first-order transfer function, where T_{pll} is the time constant; θ_g is the angle of PCC voltage vector; θ_{pll} is PLL output angle),

Applying Kirchhoff voltage laws to the circuit in Fig.1c yields:

$$\underline{U}_g^{pcc} e^{j\delta_g} = jX_c \underline{I}_c^{pll} e^{j\delta_{pll}} + \underline{U}_s \quad (1)$$

In (1), $\delta_g = \theta_g - \theta_s$ is the relative angle of the PCC voltage to the grid voltage, and $\delta_{pll} = \theta_{pll} - \theta_s$ is the relative angle of the PLL output to the grid voltage.

In accordance with assumptions c) and d), the dynamic parts of the system can be modelled as:

$$\begin{cases} T_c \dot{\underline{I}}_c^{pll} = -\underline{I}_c^{pll} + \underline{I}_c^{ref} \\ T_{pll} \dot{\theta}_{pll} = -\theta_{pll} + \theta_g \end{cases} \quad (2)$$

Hence, the reduced-order model of the VSC–grid system (ROM-VGS) constitutes (1) and (2). Normally, $T_{pll} \gg T_c$ and (2) constitutes a singular perturbed system, hence the PLL and current response are dynamically decoupled.

2.3 Analysis of the normal interactions between the VSC and grid

In this study, PCC voltage is observed for the analysis. The *d*-axis of PLL-RF is aligned with the PCC voltage in steady state; thus, the active power can be controlled by the *d*-axis current. The transition of the PCC voltage to the new equilibrium point is illustrated in Fig. 2a:

a) Phase-angle jump of the PCC voltage (*Ph. I*). If a step change in $\underline{I}_c^{ref}$ occurs, then $\underline{I}_c^{pll}$ increases with time constant T_c. Meanwhile, $\underline{U}_g^I$ rotates in the mathematically positive direction by an incremental angle $\Delta\delta_g^I$ according to (1). Given $T_c \ll T_{pll}$, in this phase, PLL remains static

($\Delta\delta_{pll}^{I}=0$).

b) Phase-angle tracking of PLL (*Ph. II*). In this phase, PLL starts rotating forward by $\Delta\delta_{pll}^{II}$ to track the angle $\Delta\delta_{g}^{I}$. Given $T_c \ll T_{pll}$, the current response is in quasi-static state and rotates with PLL simultaneously. Meanwhile, the PCC voltage adjusts its angle by $\Delta\delta_{g}^{II}$ according to (1).

c) Steady state (*Ph. III*). PLL and current dynamics settle to a new equilibrium point $\delta_{g0}^{II}=\delta_{pll0}^{II}$.

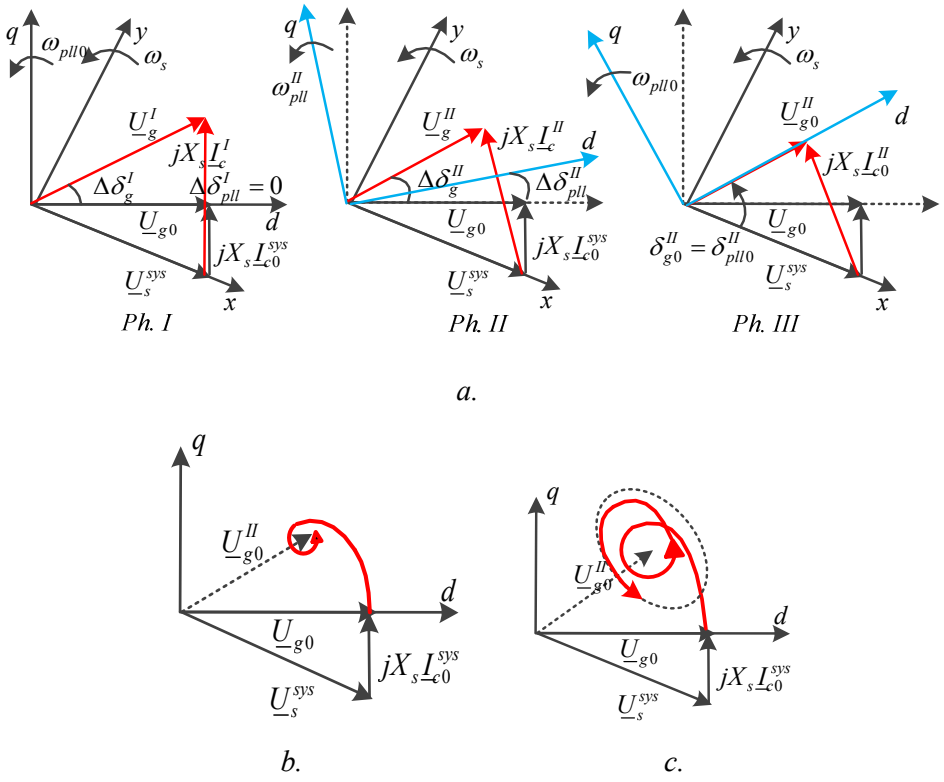

Fig. 2. *Phasor analysis of the PCC voltage dynamics (figures are exaggerated for clear demonstration)*
a. Split actions of the PCC voltage dynamics
b. Phase portrait of the PCC voltage under strong grid conditions
c. Phase portrait of the PCC voltage under weak grid conditions

According to the foregoing analysis, the phase portrait of the PCC voltage can be drew in Fig.2b. It shows a well-damped trajectory due to the decoupled characteristic of current and PLL response under strong grid conditions. However, if the grid is weak, the trajectory of the PCC voltage may be oscillatory as Fig. 2c depicted. To investigate this, a detailed model is needed and modelled in Section 3.

3. Dynamic properties of the VSC under weak grid conditions

3.1 Switch-averaged model of the VSC–grid system

For the analysis of control interactions, switching effects are usually eliminated by averaging the modulation signals along the switching period. This leads to a switch-averaged model of the VSC–grid system (SAM-VGS), and the following characteristics should be included:

a) Nonideal current source characteristic of the VSC. The output admittance $\mathbf{Y}_c(s)$ in Fig. 1b should be modelled.

b) Grid model should be modelled as impedance in accordance with requirement a).

c) The angle difference from PCC voltage to the grid should be reflected.

In this case, the *dq* impedance model in [7] and [13] can be used. However, as mentioned in Section.1, the properties of interactions are lost. Thus, the complex phasor method [27] is adopted to gain more insights into the internal properties.

Fig. 3a presents the equivalent circuit in accordance with the above modelling requirements.

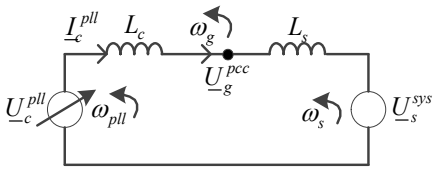

a.

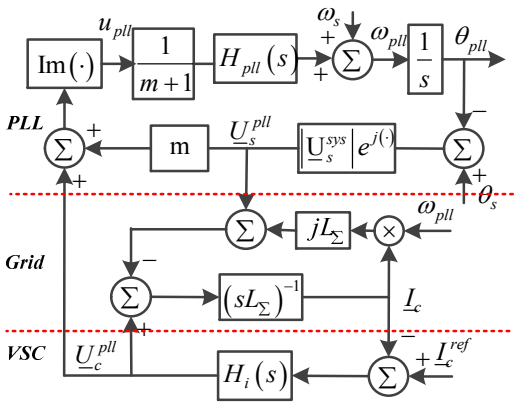

b.

This article has been accepted for publication in a future issue of this journal, but has not been fully edited.
Content may change prior to final publication in an issue of the journal. To cite the paper please use the doi provided on the Digital Library page.

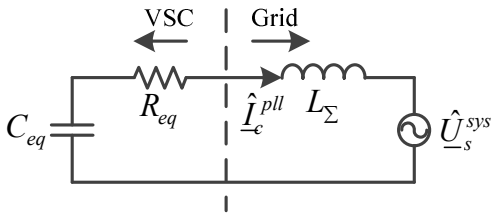

c.

Fig.3 *Equivalent circuit and model of the VSC–grid system under weak grid conditions*

a. Equivalent circuit of the VSC–grid system for weak grid analysis

b. SAM–VGS for weak grid interaction analysis

c. RLC equivalent circuit of the VSC–grid system

Applying Kirchhoff voltage law to the circuit in Fig3a yields:

$$\underline{U}_c^{pll}=L_\Sigma\frac{d\underline{I}_c^{pll}}{dt}+j\omega_{pll}L_\Sigma\underline{I}_c^{pll}+\underline{U}_s^{sys}e^{j\left(\theta_s-\theta_{pll}\right)}. \quad (3)$$

In (3), $\underline{U}_c^{pll}=U_{cd}^{pll}+j\cdot U_{cq}^{pll}$, $\underline{U}_s^{sys}=U_s^{sys}+j\cdot 0$ when the *d*-axis of the SRF is aligned with $\underline{U}_s^{sys}$, $\underline{U}_g^{pcc}=U_g^{pcc}+j\cdot 0$ when the *d*-axis of PCC-RF is aligned with $\underline{U}_g^{pcc}$, $\underline{I}_c^{pll}=I_{cd}^{pll}+j\cdot I_{cq}^{pll}$, and $L_\Sigma=L_c+L_s$ is the total circuit inductance.

PI controller is applied for VSC current control:

$$\begin{cases}\underline{U}_c^{pll}=k_{pc}\left(\underline{I}_c^{ref}-\underline{I}_c^{pll}\right)+\underline{x}_c\\ \dot{\underline{x}}_c=k_{ic}\left(\underline{I}_c^{ref}-\underline{I}_c^{pll}\right)\end{cases}, \quad (4)$$

where k_{pc} and k_{ic} are the proportional and integral gains of the current controller $H_i(s)$ in Fig. 1a respectively. The rules of the optimum second-order response are adopted for the PI controller design [31], consequently, $k_{pc}=2\alpha_c L_c$ and $k_{ic}=\left(\frac{\alpha_c}{\varepsilon}\right)^2 L_c$, $\varepsilon=0.707$. In this study, α_c is defined as the bandwidth, and its inverse is equivalent to the time constant of the VSC current response.

The intermediate variable $\underline{U}_g^{pcc}$ can be eliminated via:

$$\frac{\underline{U}_c^{pll}e^{j\theta_{pll}}-\underline{U}_g^{pcc}e^{j\theta_g}}{pL_c}=\frac{\underline{U}_g^{pcc}e^{j\theta_g}-\underline{U}_s^{sys}e^{j\theta_s}}{pL_s}, \quad (5)$$

where p is the differential operator, and (5) can be rewritten as follows:

$$\underline{U}_c^{pll}+m\underline{U}_s^{sys}e^{j\left(\theta_s-\theta_{pll}\right)}=(m+1)\underline{U}_g^{pcc}e^{j\left(\theta_g-\theta_{pll}\right)}. \quad (6)$$

In (6), $m = L_c / L_s$.

PLL in Fig. 1a can be modelled as:

$$\begin{cases} \dot{x}_{pll} = k_{plli} \cdot u_{pll} \\ \dot{\theta}_{pll} = \omega_{pll} \\ \omega_{pll} = k_{pllp} \cdot u_{pll} + x_{pll} + \omega_s \\ u_{pll} = \dfrac{1}{m+1}\left(U_{cq}^{pll} + m\left|\underline{U}_s^{sys}\right|\sin\left(\theta_s - \theta_{pll}\right)\right) \end{cases} \quad ,(7)$$

where k_{pllp} and k_{plli} are the proportional and integral gains of the PLL controller $H_{pll}(s)$, and x_{pll} is the state variable in PLL. The rules for designing k_{pllp} and k_{plli} are the same as that of the current controller. Therefore, $k_{pllp} = \dfrac{2\alpha_{pll}}{\left|\underline{U}_s^{sys}\right|}$ and $k_{plli} = \left(\dfrac{\alpha_{pll}}{\varepsilon}\right)^2 \cdot \dfrac{1}{\left|\underline{U}_s^{sys}\right|}$, where α_{pll} is the closed-loop bandwidth of PLL.

The mathematic model of SAM–VGS constitutes (3)–(7). The corresponding block diagram is shown in Fig. 3b.

3.2 IOP in the VSC–grid system

3.2.1 RLC equivalent circuit of the VSC–grid system: By applying the harmonic linearization method [8] to (3) and (4) of SAM-VG with the PLL impacts disregarded temporarily, the following equations can be obtained at frequency ω:

$$\hat{\underline{U}}_c^{pll} = j\left(\omega + \omega_s\right) L_\Sigma \cdot \hat{\underline{I}}_c^{pll} + \hat{\underline{U}}_s^{sys} \quad ,(8)$$

$$\hat{\underline{U}}_c^{pll} = -H_i\left(j\omega\right) \cdot \hat{\underline{I}}_c^{pll} = -\left(k_{pc} + \frac{k_{ic}}{j\omega}\right) \cdot \hat{\underline{I}}_c^{pll} \quad ,(9)$$

$$0 = \left(R_{eq} + \frac{1}{j\omega C_{eq}} + j\left(\omega + \omega_s\right) L_\Sigma\right) \cdot \hat{\underline{I}}_c^{pll} + \hat{\underline{U}}_s^{sys} \quad ,(10)$$

in (10), $R_{eq} = k_{pc} = 2\alpha_c L_c$ and $C_{eq} = \dfrac{1}{k_{ic}} = \dfrac{1}{2\alpha_c^2 L_c}$. The RLC equivalent circuit based on (10) is illustrated in Fig. 3c. It shows that even if the physical circuit does not present resistance, the proportional part of the current controller exerts a virtual resistance effect, whereas the integral part of the current controller functions as a capacitance. This property is known as the *virtual passive resistance effects* of the VSC.

3.2.2 Analytical solution of the IOP and its properties: The IOP is calculated by finding the frequency in which the imaginary part of the RLC impedance in (10) is equal to zero. Consequently, the positive

sequence resonance frequency in the SRF is:

$$\omega_{osc}^{p}=\frac{-\omega_s+\sqrt{\omega_s^2+4\cdot\left(\frac{\alpha_c}{\varepsilon}\right)^2\cdot\frac{L_c}{L_\Sigma}}}{2},\quad(11)$$

and the negative sequence resonance frequency in SRF is:

$$\omega_{osc}^{n}=\frac{\omega_s+\sqrt{\omega_s^2+4\cdot\left(\frac{\alpha_c}{\varepsilon}\right)^2\cdot\frac{L_c}{L_\Sigma}}}{2}.(12)$$

According to (11) and (12), IOP has two resonances in the SRF, i.e. ω_{osc}^{n} (Mode1) and ω_{osc}^{p} (Mode2). PF [19] analysis is performed to determine the most vulnerable mode under weak grid conditions (SCR is 2 in this study, $k_{sc}=2$). The results are shown in Table 1, it illustrates that Mode1 is well damped and more related to the current (PF of I_c is nearly equal to 1), whereas Mode 2 is less damped and more related to the current controller (PF of x_c nearly equal to 1). Therefore, ω_{osc}^{p} is more likely to oscillate than ω_{osc}^{n}.

Table 1 PF analysis ($\alpha_c=200Hz, k_{sc}=2$)

State Variables	Mode 1	Mode 2
	$-60.33+351.1j$	$-6.34+36.89j$
PF of I_c	0.914	0.096
PF of x_c	0.096	0.914

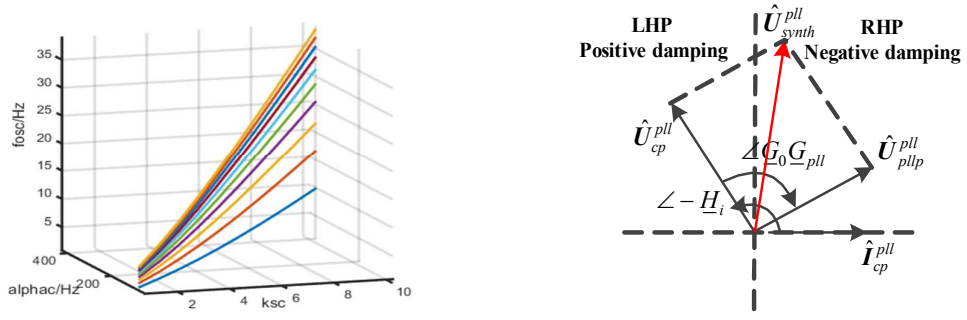

a. *b.*

Fig. 4 *a. Influence of the PLL bandwidth and SCR on IOP*
b. Phasor diagram of the damping characteristic analysis

In Fig. 4a, the frequencies of IOP are calculated with varying SCR and current controller bandwidth,

the following conditions are considered: 1) a typical value of the switching frequency for a megawatt-level VSC is approximately f_s=2 kHz. This limits the current controller bandwidth approximately to $\alpha_c \le (1/5)\cdot f_s \approx 400Hz$. 2) As mentioned in Section 2.1, the leakage inductance (e.g., L_T=0.1pu in this study) of the step-up transformer contributes to the SCR and limits the SCR to 10. Under this condition, the calculated frequency of IOP is normally below 50Hz. However, compared with the SSO in conventional power system, the existence of IOP is due to the *virtual passive element effects* of VSC, therefore, *electrical oscillation* is adopted to emphasize the control interactions.

Additionally, the given analysis suggests that the RLC equivalent of the VSC–grid system is always stable as a result of the positive resistance effects introduced by the current controller. However, a negative resistance effect can occur if the PLL interference is further considered.

3.3 Damping analysis and CSC

In this section, the damping characteristic of PLL at IOP is analysed using the SAM-VGS model and the complex phasor approach [28].

3.3.1 Complex phasor model of the VSC–grid system: Linearizing (3) and transforming all the related variables into the phasor domain yields:

$$\underline{Z}_\Sigma \cdot \hat{\underline{\mathbf{I}}}_c^{pll} = \hat{\underline{\mathbf{U}}}_c^{pll} + j\underline{U}_{s0}^{pll}\hat{\boldsymbol{\delta}}_{pll} - j\hat{\boldsymbol{\omega}}_{pll}\underline{L}_\Sigma \underline{I}_{c0}^{pll} \quad (13)$$

Where $\underline{U}_{s0}^{pll} = \underline{U}_s^{sys} e^{-j\delta_{pll0}}$, $\underline{Z}_\Sigma = j(\omega+\omega_s)\underline{L}_\Sigma$, $\hat{\underline{\mathbf{U}}}_c^{pll} = -\underline{H}_i \cdot \hat{\underline{\mathbf{I}}}_c^{pll}$, and $\underline{H}_i = \underline{H}_i(\omega)$ is the complex gain of the current controller at the perturbation frequency ω. Furthermore, $\hat{\underline{\mathbf{I}}}_c^{pll} = \hat{\mathbf{I}}_{cd}^{pll} + j\cdot\hat{\mathbf{I}}_{cq}^{pll}$ is the current complex phasor at ω, where $\hat{\mathbf{I}}_{cd}^{pll}$ and $\hat{\mathbf{I}}_{cq}^{pll}$ are the *d*- and *q*-axis current phasors; $\hat{\underline{\mathbf{U}}}_c^{pll} = \hat{\mathbf{U}}_{cd}^{pll} + j\cdot\hat{\mathbf{U}}_{cq}^{pll}$ is the VSC output voltage complex phasor at ω, where $\hat{\mathbf{U}}_{cd}^{pll}$ and $\hat{\mathbf{U}}_{cd}^{pll}$ are the *d*- and *q*-axis voltage phasors. In Section 3.2, ω_{osc}^{p} is the more vulnerable mode; thus, only the positive sequence perturbation is considered. In this case, the *d*-axis variables always lead the *q*-axis variables by 90°. Therefore, $\hat{\mathbf{I}}_{cq}^{pll} = -j\hat{\mathbf{I}}_{cd}^{pll}$ and $\hat{\underline{\mathbf{I}}}_c^{pll} = \hat{\mathbf{I}}_{cp}^{pll} = \hat{\mathbf{I}}_{cd}^{pll}$. Similarly, the voltage can be expressed as $\hat{\underline{\mathbf{U}}}_c^{pll} = \hat{\mathbf{U}}_{cp}^{pll} = \hat{\mathbf{U}}_{cd}^{pll}$.

Linearizing (6) and (7) and transforming all the related variables into the phasor domain yield:

$$\begin{cases} \hat{\boldsymbol{\delta}}_{pll} = \underline{G}_{pll}\,\mathrm{Im}\left\{\hat{\underline{\mathbf{U}}}_c^{pll}\right\} = -\dfrac{j}{2}\underline{G}_{pll}\hat{\mathbf{U}}_{cp}^{pll} \\ \hat{\boldsymbol{\omega}}_{pll} = j\omega\cdot\underline{G}_{pll}\,\mathrm{Im}\left\{\hat{\underline{\mathbf{U}}}_c^{pll}\right\} = \dfrac{\omega}{2}\cdot\underline{G}_{pll}\hat{\mathbf{U}}_{cp}^{pll} \end{cases}, \quad (14)$$

Where $\underline{G}_{pll}=\dfrac{\underline{H}_{pll}}{m\left|\underline{U}_{s0}^{sys}\right|\cos\delta_{pll0}\cdot\underline{H}_{pll}+j\omega(m+1)}$ is the complex gain of the PLL, and $\underline{H}_{pll}=\underline{H}_{pll}(\omega)$ is the complex gain of PLL controller.

The complex phasor model of the VSC–grid system constitutes (13) and (14).

3.3.2 CSC calculation: Substituting (14) into (13) yields

$$\underline{Z}_{\Sigma}\cdot\hat{\mathbf{I}}_{cp}^{pll}=\hat{\mathbf{U}}_{synth}^{pll}=\hat{\mathbf{U}}_{cp}^{pll}+\underline{G}_{0}\cdot\underline{G}_{pll}\hat{\mathbf{U}}_{cp}^{pll},(15)$$

where $\underline{G}_{0}=\dfrac{1}{2}\left(\underline{U}_{s0}^{pll}-j\omega L_{\Sigma}\underline{I}_{c0}^{pll}\right)$ and is depend on the actual operation point; $\hat{\mathbf{U}}_{cp}^{pll}=-\underline{H}_{i}\cdot\hat{\mathbf{I}}_{cp}^{pll}$ is the damping and synchronising voltage of VSC current controller; $\hat{\mathbf{U}}_{pllp}^{pll}=\underline{G}_{0}\cdot\underline{G}_{pll}\hat{\mathbf{U}}_{cp}^{pll}$ has a similar physical meaning, $\hat{\mathbf{U}}_{synth}^{pll}$ is the synthesis voltage of the current controller and PLL.

The key factors inducing the electrical oscillations are the net damping presented by the synthesized voltage $\hat{\mathbf{U}}_{synth}^{pll}$ (Fig. 4b) on the currents. The net damping is positive if $\hat{\mathbf{U}}_{synth}^{pll}$ lies in the left half plane (LHP). On the contrary, the net damping is negative if $\hat{\mathbf{U}}_{synth}^{pll}$ lies in the right half plane (RHP). Therefore, the stability condition is:

$$\mathrm{Re}\left\{\underline{H}_{i}\left(1+\underline{G}_{0}\underline{G}_{pll}\right)\right\}\geq 0,(16)$$

CSC is the condition when imposing equality to (16). The next objective is to obtain CSC analytically.

3.3.3 Damping characteristics of the current controller: it can be studied by the magnitude and phase characteristics of $\underline{H}_{i}$:

$$\begin{cases}\angle\underline{H}_{i}=\arctan\dfrac{k_{ic}}{k_{pc}\omega_{osc}}\\ \left|\underline{H}_{i}\right|=\sqrt{k_{pc}^{2}+\left(\dfrac{k_{ic}}{\omega_{osc}}\right)^{2}}\end{cases}.(17)$$

Based on (17), Fig. 5a presents multiple curves of $\underline{H}_{i}$ with varying current controller bandwidth and SCR. At a low grid SCR (k_{sc}) value, the phase lag of $\underline{H}_{i}$ is large, and at a given current control bandwidth (α_{c}), the phase lag of $\underline{H}_{i}$ is decreasing as k_{sc} is increasing. Due to $\angle\underline{H}_{i}$ is always in the range of [−90deg, 90deg] with the configurations discussed in section 3.2.2, thus, it may concludes that the

This article has been accepted for publication in a future issue of this journal, but has not been fully edited.
Content may change prior to final publication in an issue of the journal. To cite the paper please use the doi provided on the Digital Library page.

current controller consistently provides positive damping at the IOP.

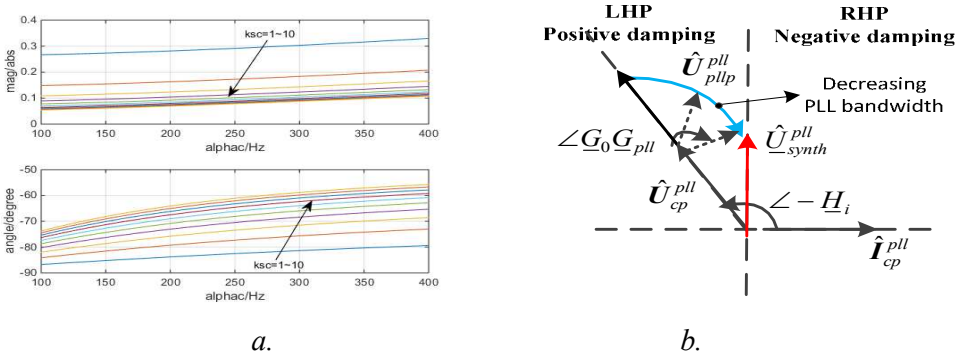

a. *b.*

Fig.5 *a. Magnitude and phase characteristics of the current controller*

b. Damping characteristics of PLL at the IOP

3.3.4 Damping characteristics of the PLL at the IOP: It is equivalent to study how the complex gain $\underline{G}_0\underline{G}_{pll}$ shapes the voltage $\hat{\mathbf{U}}_{cp}^{pll}$ in complex plane. $\underline{G}_{pll}$ is similar to a second order low-pass filter as given in (14), on the assumption of a light-load condition ($\underline{G}_0 \approx \frac{1}{2}\left|\underline{U}_{s0}^{pll}\right|\angle 0^\circ$), $\underline{G}_0\underline{G}_{pll}$ is mainly affected by $\underline{G}_{pll}$. The characteristics of $\underline{G}_{pll}$ can be understood by comparing IOP (ω_{osc}) with $\underline{G}_{pll}$ bandwidth ($\omega_{pll} = \alpha_{pll} / \varepsilon$). e.g., if $\omega_{pll} \ll \omega_{osc}$, the phase of $\underline{G}_{pll}$ approaches zero, while the magnitude of $\underline{G}_{pll}$ remains large, if $\omega_{pll} \gg \omega_{osc}$, the phase of $\underline{G}_{pll}$ approaches −90°, and the magnitude of $\underline{G}_{pll}$ attenuates to a relative small values. The magnitude and phase shaping effects of $\underline{G}_{pll}$ on the voltage $\hat{\mathbf{U}}_{cp}^{pll}$ is illustrated in Fig. 5b, it presents that a phase lag with sufficient large magnitude of $\underline{G}_{pll}$ may drive $\hat{\mathbf{U}}_{synth}^{pll}$ to the RHP. Therefore, additional negative damping is expected.

On the basis of the presented analysis, there exists a critical α_{pll} satisfies the net damping is zero ($\hat{\mathbf{U}}_{synth}^{pll}$ is orthogonal to $\hat{\mathbf{I}}_{c}^{pll}$). This physical interpretation is equivalent to the CSC in (16). In order to obtain an analytical solution of CSC, the following assumptions are considered according to the analysis: 1) a 90° phase shift of the current controller at IOP. 2) IOP is around $\underline{G}_{pll}$ bandwidth in order to present phase lag with sufficient large magnitude. Consequently, $\underline{G}_0\underline{G}_{pll}$ can be simplified to

$$\underline{G}_0\underline{G}_{pll}=\frac{0.5\cdot k_{pllp}}{j\omega_{osc}\left(m+1\right)}.(18)$$

CSC is satisfied when

$$ac-bd=0\ ,(19)$$

where $\underline{H}_i=a+jb$ and $1+\underline{G}_0\underline{G}_{pll}=c+jd$.

Substituting (18) into (19) yields

$$\frac{\omega_{osc}\left(m+1\right)}{0.5k_{pllp}}=\frac{k_{ic}}{k_{pc}\omega_{osc}}.(20)$$

Then, the following analytical solution of CSC is derived:

$$\alpha_{pll}^{\text{csc}}=\frac{2\varepsilon^2\omega_{osc}^2\left(m+1\right)}{\alpha_c}.(21)$$

The PLL bandwidth ($\alpha_{pll}^{\text{csc}}$) that satisfies (21) renders the system critically stable. Around $\alpha_{pll}^{\text{csc}}$, if $\alpha_{pll}>\alpha_{pll}^{\text{csc}}$, the net damping is negative, indicates an unstable system. If $\alpha_{pll}<\alpha_{pll}^{\text{csc}}$, then the net damping is positive, indicates a stable system. This conclusion is based on the small-signal assumption. Influences of nonlinearities are addressed in the simulation section.

In summary, the occurrence of electrical oscillations can be elucidated as follows: an IOP (11) lies in the VSC–grid system because of the virtual passive element effect of the VSC. The net damping is negative if the PLL bandwidth is above the value given by the analytical solution of CSC in (21).

4. Stability control for the VSC

Electrical oscillations as discussed above, if not properly controlled, may lead to the disconnection of RPG systems. In this section, a stabiliser called VSC-based power system stabiliser (VPSS) is proposed. The functionality of the VPSS is similar to that of the power system stabiliser (PSS) for synchronous generators.

4.1 Stability control by shaping $\underline{G}_0$

In Section 3.3.4, the damping characteristics of the PLL are analysed under the no-load or light-load condition of the VSC. However, $\underline{G}_0$ may change the property to some extents if the VSC operates in

different modes. As shown in Fig. 6a, the complex gain $\underline{G}_0$ has a lagging phase angle in the inverter mode. This condition leads to the rotation of $\hat{\mathbf{U}}_{pllp}^{pll}$ (Fig. 5b) in the mathematically negative direction, which is equivalent to negative damping. On the contrary, $\underline{G}_0$ has leading phase characteristics in the rectifier mode (Fig. 6b), and $\hat{\mathbf{U}}_{pllp}^{pll}$ consequently rotates in the mathematically positive direction, and positive damping is expected. Normally all the RPG applications with VSCs require inverter-mode operation; consequently, these applications are susceptible to electrical oscillation issues.

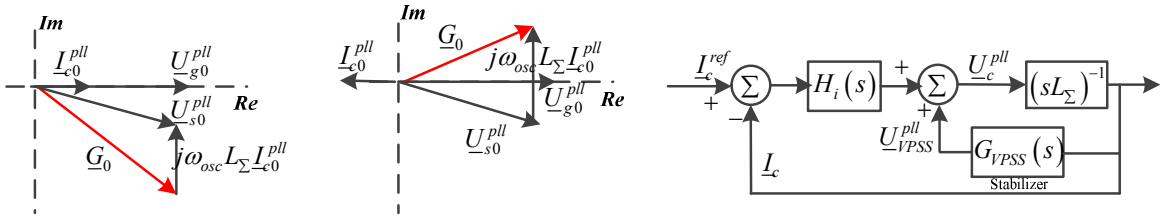

a. *b.* *c.*

Fig.6 *a. Phasor diagram of* $\underline{G}_0$ *under unit PF inverter operation*
b. Phasor diagram of $\underline{G}_0$ *under unit PF rectifier operation*
c. Control block with stabiliser for the VSC

4.2 Stability control by adding a stabiliser

The band-pass filter $G_{VPSS}=\dfrac{K_{VPSS}\cdot T_2 s}{(T_1 s+1)(T_2 s+1)}$ is aimed to provide additional damping at the IOP, advanced design of VPSS is not in the scope of the study. In this filter, T_2 is the time constant selected for DC attenuation, T_1 is the time constant selected for filtering out high frequencies (in this study is the fundamental frequency), and K_{VPSS} is the amount of damping. Fig. 6c shows that the input of the stabiliser is current, and its output is an additional voltage component added to the original output voltage. The stabiliser effectively introduces the *virtual resistance* K_{VPSS} into the circuit within its bandwidth. In general, the proposed stabiliser can be regarded as the impedance-shaping method in [7].

5. Simulation verification and discussion

The VSC–grid test system in Fig. 1a is constructed in PSCAD/EMTDC software with a switching VSC model. The parameter values are given in Table 2.

Table 2 Parameter values of the simulation model

Equipment	Parameter: Value
VSC	Rated power of VSC, S_c: 2 MW
	Rated voltage of VSC, U_c: 0.69 kV
	Input inductance, L_c: 0.1 p.u.
IGBT switch	Switching frequency: 2.4 kHz
DC link	DC rated voltage, E_{dc}: 1.1 kV
Step-up transformer	Rated capacity, S_T: 2 MVA
	Turns ratio, N: 0.69/35 kV
	Leakage inductance, L_T: 0.1 p.u.
Equivalent grid	SCR, k_{sc}: 2–10
	Equivalent inductance, L_s: (1/k-L_c) p.u.
	Grid voltage grid, U_s: 35 kV

5.1 Property of the electrical oscillations and CSC verification

Scenario 1. The VSC is under no-load condition, SCR is two ($k_{sc}=2$), and the current controller bandwidth is $\alpha_c = 200Hz$. The IOP calculated by (11) is $f_{osc} = 6.02Hz$. The bandwidth of PLL that satisfies the CSC given by (21) is $\alpha_{pll} = 8.61Hz$. This condition has been verified in the simulation by inputting the calculated values of α_{pll} and α_c into the test system. The results are shown in Fig. 7 (FFT configurations: sampling rate is f_s = 1 kHz; time frame is T = 5 s; simulation step is h = 10 μs).

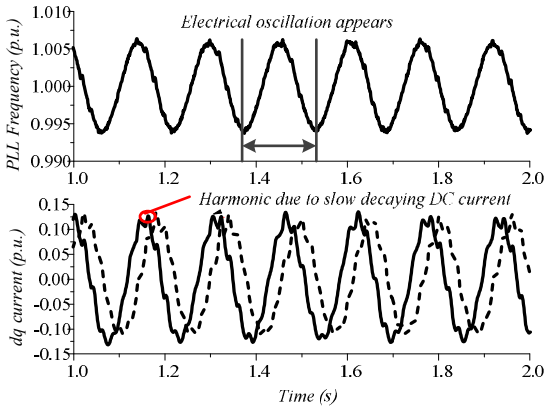

a.

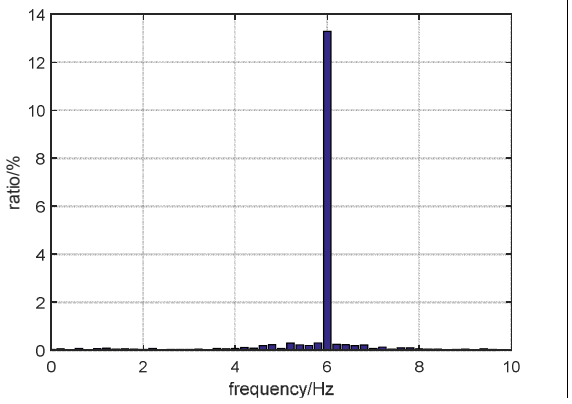

b.

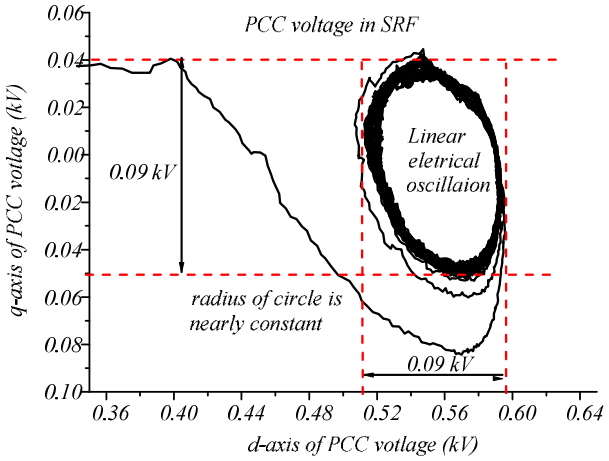

c.

Fig.7. *Simulation waveforms for scenario 1*

a. d-Axis (solid line) and q-axis (dashed line) current and PLL frequency waveforms

b. FFT analysis of the d-axis current

c. Phase portrait of the PCC voltage

Fig. 7a shows that electrical oscillations occur as predicted. This result proves that (21) accurately determined the marginally stable operation point. Fig. 7b proves that the IOP is accurately predicted by (11). Fig. 7c shows the dynamic behaviour of the PCC voltage when the electrical oscillation occurs and proves the analysis in the previous section.

5.2 Performance of the VPSS and G_0 on stability control

Scenario 2. Initial system configurations are the same as in Scenario1, except that the load of VSC is changed to two modes. First, VSC initially operates at no load; then, at 3 s simulation time, the VSC is changed to a rectifier mode, with the active current reference being 1.0 *p.u.* (Mode 1). Second, the VSC

initially operates at no load; then, at 3 s simulation time, the VSC is changed to inverter mode, with the active current reference at 1.0 *p.u.* (Mode 2).

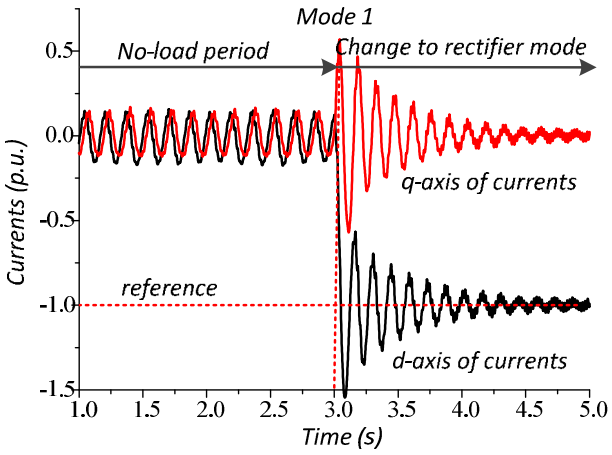

a.

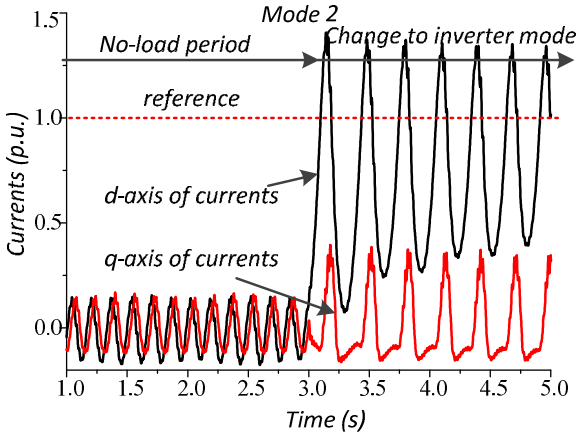

b.

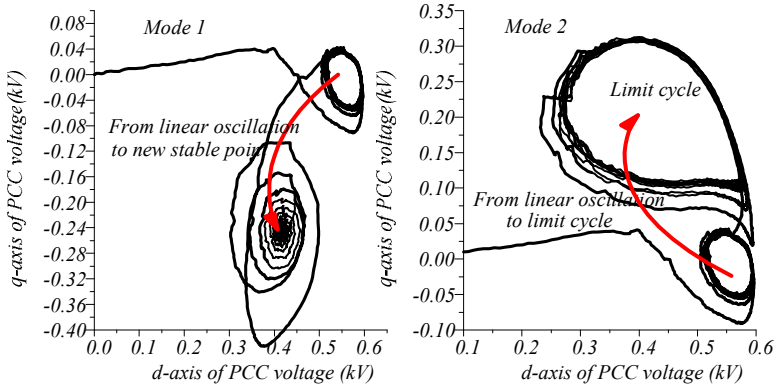

c.

Fig. 8 *Damping characteristics in different operation modes*

a. Current waveforms of Mode 1

b. Current waveforms of Mode 2

c. Phase portrait comparisons of Mode 1 and Mode 2

Fig. 8a shows that $\underline{G}_0$ has positive damping effects on the currents when the VSC is in the rectifier mode. Fig. 8b shows that large oscillations occur as a result of the negative damping effects of $\underline{G}_0$ in the inverter mode. However, the amplitude of Mode2 oscillation does not increase to infinity but is instead limited to a cycle because of the nonlinearities in the VSC (e.g. over modulation) as illustrated in Fig. 8c. This phenomenon is known as the limit cycle [32] in nonlinear system. The oscillation frequency in Mode 2 can no longer be predicted by the linear oscillation analysis in (11).

Scenario 3.The VSC is loaded with 0.5 p.u. active current (inverter mode), the SCR is two ($k_{sc}=2$), the current controller bandwidth is $\alpha_c=200Hz$. The PLL bandwidth is initially set to 5 Hz; then, at 5 s simulation time, it is set to 15 Hz. The VPSS control is activated at 6 s before the linear oscillation transitions to nonlinear, as discussed in Scenario 2. (Other conditions: K_{VPSS}=0.1; T_1=2 ms; T_2=1 s)

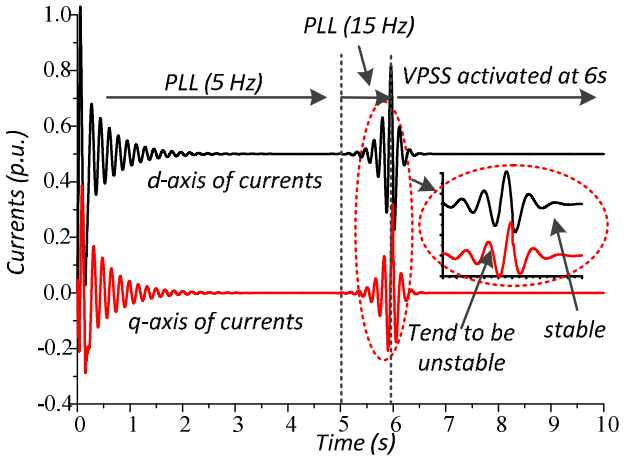

a.

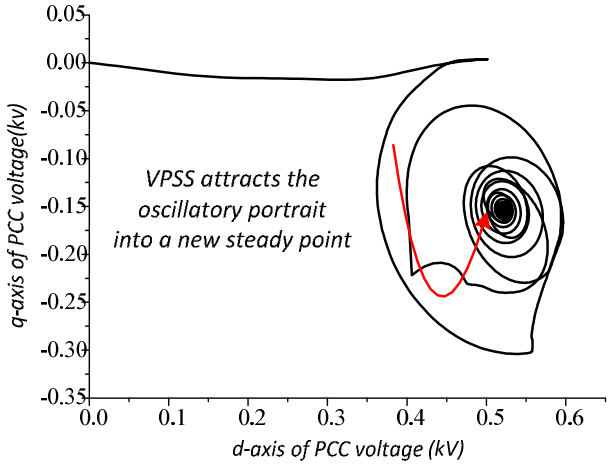

b.

Fig.9 *Performance of the stabiliser for VSC*

a. Current waveforms

b. Phase portraits of the PCC voltage

As presented in Fig. 9, before 5 s the net damping is positive and the system enters the small-signal stable state because the PLL bandwidth is below the CSC limit provided in Scenario 1. However, after 5 s, the PLL bandwidth is set higher than the CSC limit. As a result, the net damping is negative, and the system enters the small-signal unstable state. Subsequently, at 6 s, the proposed VPSS for the VSC is activated, and this stabiliser damps the oscillations efficiently, thereby ensuring system stability. Fig. 9b presents the phase portrait of the PCC voltage and shows a similar outcome.

6. Conclusion

This study reveals the mechanism of electrical oscillations in the grid-tied VSC system. The VSC with current controller introduces resistive and capacitive effects into the circuit, whereas the grid inductive, consequently the VSC–grid system is equivalent to a typical RLC circuit in terms of small signal dynamics. The RLC equivalent has an IOP by nature, and can be excited in form of oscillations if PLL bandwidth satisfies the given stability criteria referred to as CSC. In order to improve the stability of the grid-tied VSC, particularly under weak grid conditions, a stabiliser for the VSC is proposed. It essentially adds positive damping to the RLC equivalent circuit, thereby ensuring stable operation. Time domain simulations in PSCAD/EMTDC are proved that the presented analysis is valid.

Acknowledgment

This work is supported by the Power Electronics Science and Education Development Program of Delta Environmental & Educational Foundation (DREM2016005).

References

[1] Kouro, S., Leon J, I., Vinnikov, D., *et al.*: 'Grid-connected photovoltaic systems: An overview of recent research and emerging PV converter technology', IEEE Industrial Electronics Magazine, 2015, **9**, (1), pp 47–61

[2] Blaabjerg, F., Liserre, M., Ma, K.: 'Power electronics converters for wind turbine systems', IEEE Transactions on Industry Applications, 2012, **48**, (2), pp. 708–719

[3] Wang, F., Duarte J, L., Hendrix M A, M., *et al.*: 'Modeling and analysis of grid harmonic distortion impact of aggregated DG inverters', IEEE Transactions on Power Electronics, 2011, **26**, (3), pp. 786–797

[4] Liserre, M., Teodorescu, R., Blaabjerg, F.: 'Stability of photovoltaic and wind turbine grid-connected inverters for a large set of grid impedance values', IEEE Transactions on Power Electronics, 2006, **21**, (1), pp. 263–272

[5] Miao, Z.: 'Impedance-Model-Based SSR Analysis for Type 3 Wind Generator and Series-Compensated Network', IEEE Transactions on Energy Conversion, 2012, **27**, (4), pp. 984–991

[6] Varma R, K., Moharana, A.: 'SSR in double-cage induction generator-based wind farm connected to series-compensated transmission line', IEEE Transactions on Power Systems, 2013, **28**, (3), pp. 2573–2583

[7] Kunjumuhammed L, P., Pal B, C., Oates, C., *et al.*: 'Electrical Oscillations in Wind Farm Systems: Analysis and Insight Based on Detailed Modeling', Sustainable Energy, IEEE Transactions on, 2016, **7**, (1), pp. 51–62

[8] Harnefors, L., Bongiorno, M., Lundberg, S.: 'Input-admittance calculation and shaping for controlled voltage-source converters', Industrial Electronics, IEEE Transactions on, 2007, **54**, (6), pp. 3323–3334

[9] Cespedes, M., Sun, J.: 'Impedance Modeling and Analysis of Grid-Connected Voltage-Source Converters', IEEE Transactions on Power Electronics, 2014, **29**, (3), pp. 1254–1261

[10] Wen, B., Boroyevich, D., Burgos, R., *et al.*: 'Small-Signal Stability Analysis of Three-Phase AC Systems in the Presence of Constant Power Loads Based on Measured d-q, Frame Impedances', IEEE Transactions on Power Electronics, 2015, **30**, (10), pp. 5952–5963

[11] Sun, J.: 'Impedance-based stability criterion for grid-connected inverters', IEEE Transactions on Power Electronics, 2011, **26**, (11), pp. 3075–3078

[12] Burgos, R., Boroyevich, D., Wang. F., *et al.*: 'On the Ac stability of high power factor three-phase rectifiers' , ECCE, Atlanta, Georgia, USA, September 2010, pp. 2047–2054

[13] Cespedes, M., Sun, J.: 'Modeling and mitigation of harmonic resonance between wind turbines and the grid', ECCE, Phoenix, USA, September 2011, pp. 2109 –2116

[14] Dong, D., Wen, B., Boroyevich, D., *et al.*: 'Analysis of Phase-Locked Loop Low-Frequency Stability in Three-Phase Grid-Connected Power Converters Considering Impedance Interactions', IEEE Transactions on Industrial Electronics, 2015, **62**, (1), pp.10–321

[15] Wen, B., Boroyevich, D., Mattavelli, P., *et al.*: 'Influence of phase-locked loop on input admittance of three-phase voltage-source converters', Applied Power Electronics Conference & Exposition, Los Angle, USA, March 2013, pp.897–904

[16] Turner, R., Walton, S., Duke, R.: 'A case study on the application of the Nyquist stability criterion as applied to interconnected loads and sources on grids', IEEE Transactions on Industrial Electronics, 2013, 60, (7), pp.2740–2749

[17] Alawasa K, M., Mohamed Y A R, I.: 'A Simple Approach to Damp SSR in Series-Compensated Systems via Reshaping the Output Admittance of a Nearby VSC-Based System', IEEE Transactions on Industrial Electronics, 2015, **62**, (5), pp. 2673–2682

[18] Yang, D., Ruan, X., Wu, H.: 'Impedance shaping of the grid-connected inverter with LCL filter to improve its adaptability to the weak grid condition', IEEE Transactions on Power Electronics, 2014, **29**, (11), pp. 5795–5805

[19] Chaudhuri N, R., Majumder, R., Chaudhuri, B., *et al*.: 'Stability analysis of VSC MTDC grids connected to multimachine AC systems', IEEE Transactions on Power Delivery, 2011, **26**, (4), pp. 2774–2784

[20] Fernandez R, D., Mantz R, J., Battaiotto P, E.: 'Impact of wind farms on a power system. An eigenvalue analysis approach', Renewable energy, 2007, **32**, (10), pp.1676–1688.

[21] Gautam, D., Vittal, V., Harbour, T.: 'Impact of increased penetration of DFIG-based wind turbine generators on transient and small signal stability of power systems', IEEE Transactions on Power Systems, 2009, **24**, (3), pp. 1426–1434

[22] Díaz, G., González-Morán, C., Viescas, C.: 'State-space representation of DFIG-based wind power plants', IET Renewable Power Generation, 2013, **7**, (3), pp. 254–264

[23] Mohammadpour H, A., Ghaderi, A., Santi, E.: 'Analysis of sub-synchronous resonance in doubly-fed induction generator-based wind farms interfaced with gate–controlled series capacitor', IET Generation Transmission & Distribution, 2014, **8**, (12), pp. 1998–2011

[24] Johnson A, I., Barney J, R.: ' Numerical Methods for Differential Systems ' (Academic Press Inc., New York, 2014), pp. 97–124

[25] Céspedes, M., Sun, J.: ' Online grid impedance identification for adaptive control of grid-connected inverters' , ECCE, NC, USA , September 2012, pp. 914–921

[26] Roinila, T., Vilkko, M., Sun, J.: 'Online grid impedance measurement using discrete-interval binary sequence injection', Emerging and Selected Topics in Power Electronics, 2014, **2**, (4), pp. 985–993

[27] Wen, B., Boroyevich, D., Mattavelli, P., *et al*.: 'Experimental verification of the generalized Nyquist stability criterion for balanced three-phase AC systems in the presence of constant power loads', ECCE, NC, USA, September 2012, pp. 3926–3933

[28] Chen, H., Guo C, L., Chen Q, L.: 'Sub-Synchronous Oscillation Caused by HVDC and the Damping Characteristic Analysis', Advanced Materials Research, Hong Kong, China, August 2014, pp. 1353–1356

[29] Zheng Xu.: 'The Complex Torque Coefficient Approach's Applicability Analysis and its Realization by Time Domain Simulation', Proceedings of the CSEE, 2000,**20**, 6, pp. 1–4

[30] Tabesh, A., Iravani, R.: 'On the application of the complex torque coefficients method to the analysis of torsional dynamics', IEEE Transactions on Energy Conversion, 2005, **20**, (2), pp. 268–275

[31] Zhu, X., Sun, H., Wen, J., *et al*.: 'Improved Complex Torque Coefficient Method Using CPCM for Multi-Machine System SSR Analysis', IEEE Transactions on Power Systems, 2014, **29**, (5), pp. 2060–2068

[32] Dorf, R., Bishop, R.: 'Modern Control Systems 7th Edition'(Addison-Wesley. 1995)

[33] Khalil H, K., Grizzle J, W.: 'Nonlinear systems '(New Jersey, Prentice hall. 1996)